Published in final edited form as:

Nat Microbiol. 2018 October ; 3(10): 1131–1141. doi:10.1038/s41564-018-0229-0.

Autophagy proteins suppress protective type I interferon signaling in response to the murine gut microbiota

Patricia K. Martin[1,2], **Amanda Marchiando**[1], **Ruliang Xu**[4], **Eugene Rudensky**[1,2], **Frank Yeung**[1,2], **Samantha L. Schuster**[1], **Elisabeth Kernbauer**[1], and **Ken Cadwell**[1,3]

[1]Kimmel Center for Biology and Medicine at the Skirball Institute, New York University School of Medicine, New York, NY 10016, USA

[2]Sackler Institute of Graduate Biomedical Sciences, New York University School of Medicine, New York, NY 10016, USA

[3]Department of Microbiology, New York University School of Medicine, New York, NY 10016, USA

[4]Department of Pathology, New York University School of Medicine, New York, NY 10016, USA

Abstract

As a conserved pathway that lies at the intersection between host defense and cellular homeostasis, autophagy serves as a rheostat for immune reactions. In particular, autophagy suppresses excess type I interferon (IFN-I) production in response to viral nucleic acids. It is unknown how this function of autophagy relates to the intestinal barrier where host-microbe interactions are pervasive and perpetual. Here, we demonstrate that mice deficient in autophagy proteins are protected from the intestinal bacterial pathogen *Citrobacter rodentium* in a manner dependent on IFN-I signaling and nucleic acid sensing pathways. Enhanced IFN-stimulated gene (ISG) expression in intestinal tissue of autophagy-deficient mice in the absence of infection was mediated by the gut microbiota. Additionally, monocytes infiltrating into the autophagy-deficient intestinal microenvironment displayed an enhanced inflammatory profile and were necessary for protection against *C. rodentium*. Finally, we demonstrate that the microbiota-dependent IFN-I production that occurs in the autophagy-deficient host also protects against chemical injury of the intestine. Thus, autophagy proteins prevent a spontaneous IFN-I response to microbiota that is beneficial in the presence of infectious and non-infectious intestinal hazards. These results identify a role for autophagy proteins in controlling the magnitude of IFN-I signaling at the intestinal barrier.

*To whom correspondence should be addressed: Ken Cadwell, Ph.D. New York University School of Medicine, ACLS-WT 409, 430 East 29th Street, New York, NY 10016, USA. Telephone: (212) 263-8891. Fax: (212) 263-5711. ken.cadwell@med.nyu.edu.

Author Contributions

P.K.M., A.M., and K.C. formulated the original hypothesis, designed the study, and analyzed the results. E.R. assisted with the transcriptomics analyses. R.X. performed histopathology analyses. E.K. assisted with experiments involving GF mice. S.L.S. and F.Y. assisted with analyses of microbial communities. P.K.M. and K.C. wrote the manuscript, and all authors commented on the manuscript, data, and conclusions.

Competing financial interests

The authors declare no competing financial interests.

INTRODUCTION

The trillions of bacteria and other infectious agents in the gastrointestinal tract are a constant source of immunostimulatory ligands. Although products originating from the microbiota benefit the host by inducing leukocyte differentiation, an unrestrained response is implicated in the chronic intestinal inflammation characteristic of inflammatory bowel disease (IBD). Mucins, antimicrobial peptides, and immunoglobulins create separation between the epithelium and luminal bacteria, but microbial ligands can pass through this barrier and activate the immune system at both local and distal sites[1]. Elucidating cell-intrinsic mechanisms that prevent hyperactivation of the innate immune system is key to understanding how a tolerogenic environment is maintained.

The cellular pathway of autophagy (macroautophagy) is mediated by the coordinated action of conserved autophagy proteins and involves the sequestration of cytosolic material within a double membrane-bound vesicle termed the autophagosome. The contents, which can include organelles and protein aggregates, are degraded and recycled upon fusion of the autophagosome with the lysosome. Increasing evidence indicates that autophagy dampens inflammatory reactions by targeting immune activators and signaling molecules for degradation[2]. For instance, autophagy inhibits type I interferon (IFN-I) production in response to sensing of viral RNA and DNA in the cytosol by RIG-I and cGAS, respectively[3–8]. It is unknown whether autophagy inhibits IFN-I signaling in response to the microbiota. However, an important role for autophagy in suppressing reactions towards the gut microbiota is suggested by the association between a gene variant of *ATG16L1* and IBD susceptibility[2].

ATG16L1 forms a complex that mediates the attachment of phosphatidylethanolamine (PE) to the ubiquitin-like molecule LC3, a step that is essential for the proper formation and function of the autophagosome[2]. We previously generated mice with a germ-line gene-trap mutation that leads to decreased *Atg16L1* expression and reduced autophagy[9]. These *Atg16L1* hypomorph (*Atg16L1*^{HM}) mice develop intestinal abnormalities related to IBD upon infection with murine norovirus (MNV)[9,10], an otherwise beneficial virus that persistently infects the intestine[11]. In contrast to this pathological response to a commensal-like virus, we found that *Atg16L1*^{HM} mice are remarkably resistant to intestinal infection by the model Gram-negative bacterial pathogen *Citrobacter rodentium*[12]. This increased protection was dependent on macrophage cell types and not lymphocytes, suggesting that autophagy has a critical role in limiting innate immune responses to intestinal bacteria. Here, we show that autophagy inhibition in the intestinal epithelium confers resistance to *C. rodentium* through an enhanced IFN-I response to the microbiota.

RESULTS

Resistance conferred by Atg16L1 mutation is dependent on IFN-I

Our previous RNA deep-sequencing (RNA-Seq) experiment showed that transcripts associated with innate immunity were enriched in intestinal samples collected from *Atg16L1*^{HM} mice compared with wild-type (WT) controls[12]. Among these transcripts were IFN-I stimulated genes (ISGs), reminiscent of observations made in autophagy-deficient

tumor cells grown in culture[8,13]. To test whether this increase in IFN-I signaling mediates resistance to infection, we crossed *Atg16L1*^{HM} mice with mice that are deficient in the IFN-I receptor (*Ifnar*$^{-/-}$). *Atg16L1*^{HM} mice displayed >100 fold reductions in the number of *C. rodentium* recovered in stool following oral inoculation compared with WT controls starting around day 9 post-infection, with the greatest difference occurring at day 15 (Figure 1a,b). In contrast, bacterial burden in *Atg16L1*^{HM}*Ifnar*$^{-/-}$ mice was similar to WT and *Ifnar*$^{-/-}$ mice throughout the course of infection (Figure 1a,b), and protection from morbidity observed in *Atg16L1*^{HM} mice was lost in *Atg16L1*^{HM}*Ifnar*$^{-/-}$ mice (Figure 1c). Colonic crypt hyperplasia is associated with successful *C. rodentium* colonization[14]. *Atg16L1*^{HM} mice showed reduced levels of crypt hyperplasia and overall a lower intestinal pathology score, whereas the colons of *Atg16L1*^{HM}*Ifnar*$^{-/-}$ mice appeared similar to WT mice (Figure 1d–f). *Atg16L1*^{HM}, but not *Atg16L1*^{HM}*Ifnar*$^{-/-}$ mice, also displayed decreased *C. rodentium* dissemination to the liver (Figure 1g). These results indicate that the benefit conferred by *Atg16L1* mutation during *C. rodentium* infection is dependent on IFN-I signaling. Notably, *Ifnar*$^{-/-}$ mice displayed similar bacterial burden and modestly reduced pathology compared to WT mice (Figure 1f). This indicates that IFN-I is typically dispensable or deleterious in a WT setting, but is selectively important in *Atg16L1*^{HM} mice.

Quantification of colonic lamina propria cells by flow cytometry at day 9 post-infection did not reveal significant differences in the proportion of cytokine-producing lymphoid subsets when comparing infected WT, *Ifnar*$^{-/-}$, *Atg16L1*^{HM}, and *Atg16L1*^{HM}*Ifnar*$^{-/-}$ mice (Supplemental Figure 1a–k). We also did not observe differences among genotypes in macrophages and dendritic cells, and neutrophils displayed a modest increase in *Atg16L1*^{HM}*Ifnar*$^{-/-}$ mice (Supplemental Figure 2a–g). Because these results did not reveal an obvious shift in leukocyte populations that explains the IFN-dependent protection observed in *Atg16L1*^{HM} mice, we focused on other aspects of immunity such as the microbiota.

We incorporated littermate controls in the above experiments, but this approach does not rule out the possibility that *Ifnar* deficiency ablates the enhanced resistance conferred by *Atg16L1* mutation by reverting the microbiota of *Atg16L1*^{HM} mice to a “WT-like” state. We performed 16S rRNA sequencing of fecal microbiota isolated from mice representing the different genotypes used in this study, and included samples that were collected longitudinally from WT and *Atg16L1*^{HM} mice infected by *C. rodentium* to serve as a positive control for dysbiosis. Principal component analysis (PCA) and examination of relative abundance of various taxa showed that samples from infected WT mice diverge from the other samples that cluster together (Supplemental Figure 3a,c), similar to previous studies[14–16]. The abundance of Enterobactericiae (a family that includes *C. rodentium*) increased in WT mice during infection, and as expected based on the lower *C. rodentium* burden and crypt hyperplasia[14], was less severe in *Atg16L1*^{HM} mice (Supplemental Figure 3b). Comparison of uninfected *Atg16L1*^{HM} and *Atg16L1*^{HM}*Ifnar*$^{-/-}$ mice indicate that *Ifnar* deletion does not significantly alter the microbiota of *Atg16L1*^{HM} mice. To examine how potential microbiota differences prior to *C. rodentium* infection impact the outcome of infection, germ-free mice were inoculated with stool isolated from uninfected WT, *Atg16L1*^{HM}, *Ifnar*$^{-/-}$, and *Atg16L1*^{HM}*Ifnar*$^{-/-}$ mice, which were then infected with C. *rodentium*. We did not detect differences in bacterial burden or morbidity when comparing

mice reconstituted with microbiota from different genotypes (Supplemental Figure 3d–f). These results indicate that host genotype, and not initial differences in microbiota composition, is the dominant determinant of *C. rodentium* susceptibility.

Other models of autophagy deficiency reproduce resistance to C. rodentium infection

Next, we examined whether the effect of *Atg16L1* mutation can be reproduced by deficiency in other autophagy genes. *LC3b*$^{-/-}$ mice that are deficient in one of several LC3 paralogs displayed reduced bacterial burden compared with WT controls (Figure 2a,b). Recent studies have uncovered an innate immune function of ATG16L1 referred to as Targeting of AutophaGy proteins (TAG), which involves recruiting IFN-inducible GTPases to membranes associated with parasite replication and occurs independently of the autophagy protease ATG4B[17,18]. *Atg4b*$^{-/-}$ mice displayed an immense reduction in bacterial burden and were resistant to weight loss and other signs of disease (Figure 2c,d and Supplemental Figure 4a,b). Therefore, susceptibility to *C. rodentium* is unlikely to be mediated by TAG. The accelerated reduction in bacteria burden may reflect the more severe reduction in autophagy displayed by *Atg4b*$^{-/-}$ mice than *LC3b*$^{-/-}$ mice[19–22].

Deletion of *Atg7* or *Atg16L1* in the intestinal epithelium were reported to confer susceptibility to *C. rodentium*[23,24], which initially led us to investigate the role of ATG16L1 in the hematopoietic compartment. However, deletion of *Atg16L1* in myeloid cells (*Atg16L1*$^{flox/flox}$*LyzM*^{Cre}) did not reproduce resistance to *C. rodentium*[12]. Although we showed that *Atg16L1* deletion in dendritic cells increases T cell alloreactivity[25], the same *Atg16L1*$^{flox/flox}$*Cdllc*^{Cre} mice used in these studies displayed a similar response to *C. rodentium* infection as *Atg16L1*$^{flox/flox}$ control mice (Figure 2e,f). In contrast, mice in which *Atg16L1* is deleted in the intestinal epithelium (*Atg16L1*$^{flox/flox}$*Villin*^{Cre}) showed a significant decrease in bacterial burden (Figure 2g,h). It is possible that the discrepancy between our findings and the literature are due to differences in the health status of mice, particularly the presence of MNV which we actively exclude from our mouse colonies and showed alters immunity in *Atg16L1*$^{flox/flox}$*Villin*^{Cre} mice[26], explains the discrepancy between our findings and the literature.

The T300A variant of ATG16L1 associated with IBD introduces a caspase-3 cleavage site in the protein[27–30]. Homozygous knock-in mice harboring the equivalent variant (*Atg16L1*^{T316A}) display a potential compensatory increase in ATG16L1 compared with WT. However, we observed that full length ATG16L1 protein is decreased in *Atg16L1*^{T316A} knock-in mice orally gavaged with PAC-1, a chemical activator of caspase-3[31] (Supplemental Figure 4c). Thus, this model represents an opportunity to compare the effect of chemically-induced ATG16L1 inhibition on *C. rodentium* infection, which would avoid genotype-dependent effects on the microbiota that precede infection. We found that PAC-1-treated *Atg16L1*^{T316A} mice, but not untreated mice, phenocopied *Atg16L1*^{HM} mice by displaying decreased bacterial burden in the stool and disease compared to PAC-1 treated WT mice (Figure 2i–j and Supplemental Figure 4d). Thus, multiple animal models indicate that ATG16L1 and autophagy proteins mediate susceptibility to *C. rodentium*.

Resistance conferred by Atg16L1 mutation is mediated by MAVS accumulation

Autophagy suppresses IFN-I signaling in part through the degradation of mitochondrial antiviral signaling protein (MAVS), a signaling intermediate that aggregates at the mitochondria to activate TBK1 and IRF3 downstream of the cytosolic RNA sensors RIG-I and MDA5[6–8]. The ATG16L1 complex is recruited to mitochondria by NLRX1 and TUFM or COX5B[6,7]. We found an increase in MAVS protein in whole colonic tissue harvested from uninfected *Atg16L1*^{HM} mice compared with WT, and an increase in MAVS in whole colonic tissue from PAC-1 treated *Atg16L1*^{T316A} mice compared to PAC-1 treated WT, untreated *Atg16L1*^{T316A}, and untreated *WT* colonic tissues (Figure 3a,b,d). In the presence of cytoplasmic DNA, cGAS activates stimulator of interferon genes (STING) to signal through TBK-1 and IRF3; autophagy proteins regulate STING trafficking and availability of DNA in the cytosol[5,32–35]. We found that STING protein levels were similar in WT and *Atg16L1*^{HM} colonic tissues (Figure 3a,c). These findings are consistent with a proteomics analysis showing that MAVS, MDA5, RIG-I, IRF3, and phospho-TBK1 accumulate in *Atg5*$^{-/-}$ and *Atg7*$^{-/-}$ RAS-transformed cells, but that STING does not[8]. Also, we found that *Atg16L1*^{HM}*Mavs*$^{-/-}$ mice lose the superior protection observed in *Atg16L1*^{HM} mice (Figure 3e–g). Although STING was not increased in colonic tissue from *Atg16L1*^{HM} mice, we hypothesized that cytosolic DNA sensing could contribute to enhanced resistance because MAVS and STING share downstream signaling factors (IRF3 and TBK-1) that are activated in autophagy-deficient cells[8]. Indeed, *Atg16L1*^{HM}*Sting*$^{-/-}$ mice also lose the protection conferred by *Atg16L1* mutation (Figure 3h–j). These results indicate that sensing of cytosolic nucleic acids is necessary for the increased resistance to *C. rodentium* conferred by *Atg16L1* mutation.

Increased IFN-I signaling in Atg16L1^{HM} mice is dependent on the microbiota

Increased ISG expression in *Atg16L1*^{HM} mice is observed both before and during *C. rodentium* infection[12]. Such spontaneous activation could be explained by the microbiota. Although colons harvested from conventional *Atg16L1*^{HM} and *Atg4b*$^{-/-}$ mice displayed increased expression of *Mx2* and *Oasl2* in a manner dependent on IFNAR, the expression of these representative ISGs was reduced to WT levels in germ-free (GF) *Atg16L1*^{HM} mice (Figure 4a,b and Supplemental Figure 4f). *Mx2* expression was not increased in peripheral organs from *Atg16L1*^{HM} mice (Supplemental Figure 4e), suggesting a local response. Immunohistochemistry (IHC) analyses confirmed that phospho-STAT1 (pSTAT1), another marker of IFN-I, is detected throughout the colonic epithelium and lamina propria of conventional *Atg16L1*^{HM} and *Atg4b*$^{-/-}$ mice, and not nearly as detectable in conventional WT mice or GF WT and GF *Atg16L1*^{HM} mice (Figure 4c,d). ISGs can also induce epithelial cell proliferation[36]. We found that *Atg16L1*^{HM} and *Atg4b*$^{-/-}$ mice have an increase in Ki67^{+} proliferating colonic epithelial cells compared to WT, GF WT, and GF *Atg16L1*^{HM} mice (Figure 4e,f). These findings indicate that ATG16L1 suppresses IFN-I signaling downstream of local sensing of the microbiota.

The enhanced IFN-I response in Atg16L1 mutant mice protects against tissue injury

C. rodentium is avirulent in GF mice[37]. Thus, we wished to use a non-infectious model of intestinal injury to investigate the functional consequence of microbiota-induced IFN-I

signaling in the gut. We found that *Atg16L1*^{HM} mice receiving the intestinal damaging agent dextran sodium sulfate (DSS) in the drinking water displayed a striking reduction in lethality and weight loss compared with WT mice (Figure 5a,b). In contrast, GF *Atg16L1*^{HM} and GF WT mice were equally susceptible to DSS, even at a lower dose where survival is prolonged (Figure 5a and Supplemental Figure 4g). *Atg16L1*^{HM}*Mavs*$^{-/-}$ mice displayed increased lethality and similar weight loss compared with *Mavs*$^{-/-}$ controls (Figure 5c,d). Also, *Atg16L1*^{HM}*Sting*$^{-/-}$ mice displayed similar lethality compared with *Sting*$^{-/-}$ mice (Figure 5e,f). Thus, *Atg16L1* mutation protects from DSS-induced injury in a MAVS, STING, and microbiota-dependent manner.

Resistance conferred by Atg16L1 mutation is dependent on CCR2

We previously demonstrated that depletion of myeloid cells with chlodronate-loaded liposomes abrogates the enhanced resistance to *C. rodentium* displayed by *Atg16L1*^{HM} mice[12]. This observation may reflect the essential role of CD11b^{+}Ly6C^{hi} monocytes recruited to the intestine through the chemokine receptor CCR2[38]. However, *Atg16L1*$^{flox/flox}$*LyzM*^{Cre} mice that are autophagy-deficient in myeloid cells are not resistant to *C. rodentium*[12], and we did not detect a difference in the number of CD11b^{+}Ly6C^{hi} monocytes in the colons of *Atg16L1*^{HM} and WT mice (Supplemental Figure 5a,b). Additionally, the IFN signature precedes monocyte recruitment because it is detectable in the absence of *C. rodentium* infection (Figure 4a,b). Therefore, the key role of monocytes identified in our previous study appears to be at odds with the findings in this manuscript implicating ATG16L1 function in the intestinal epithelium.

One possible explanation is that properties of infiltrating monocytes, rather than their quantity, are altered upon recruitment into the *Atg16L1* mutant colon. RNA-Seq analysis of FACS-purified CD11b^{+}Ly6C^{hi} monocytes from the colon on day 9 post-infection identified 812 genes with altered expression between *Atg16L1*^{HM} and WT mice, many of which have known functions in myeloid cell differentiation and function (Figure 6a, Supplemental Figure 6, and Table S1). Pathway analyses highlighted an enrichment in genes associated with metabolism, immune signaling, and cell cycle regulation (Figure 6b). The metabolic signatures and cell cycle regulation may reflect enhanced differentiation into macrophages involved in resolution of infection and tissue repair[39]. Among the genes that were upregulated in monocytes harvested from *Atg16L1*^{HM} mice were several associated with antimicrobial responses (Supplemental Figure 6). These results indicate that monocytes that migrate to the colon during *C. rodentium* infection acquire an altered gene expression profile in an *Atg16L1* mutant setting.

To validate gene expression data, we identified three surface receptors that were increased at the RNA level in monocytes derived from *Atg16L1*^{HM} mice that were assigned to the pathway *inflammation and monocyte function* (Supplemental Figure 6): XCR1, Galectin-9, and MHC-II. All three receptors were increased on the cell surface of CD11b^{+}Ly6C^{hi} monocytes from day 9 infected *Atg16L1*^{HM} mice (Supplemental Figure 5c). We next tested whether enhanced inflammasome activation leads to increased *C. rodentium*. ATG16L1 is a potent inhibitor of NLRP3 inflammasome activity in monocytic cells[40], but we found NLRP3 to be dispensable for the protective effect of *Atg16L1* mutation (Supplemental

Figure 5d–e). However, inflammasome complexes may function in a redundant manner during *C. rodentium* infection[41], and the inflammasome gene *Nlrc4* showed increased expression in infected *Atg16L1*^{HM} mice (Supplemental Figure 6 and Table S1). Therefore, we crossed *Atg16L1*^{HM} mice with *Caspase1.11*$^{-/-}$ double knock out mice to generally inhibit inflammasomes. We found that *Atg16L1*^{HM} *Caspase1.11*$^{-/-}$ mice have similar bacterial burdens and disease scores as WT and *Caspase1.11*$^{-/-}$ controls and do not display the superior protection observed in *Atg16L1*^{HM} mice (Supplemental Figure 5f–h). Thus, although we identified an epithelial-intrinsic function of ATG16L1 linked to IFN-I signaling, other cell types and immune processes also acquire a heightened state of activity during *C. rodentium* infection.

To demonstrate that CD11b^{+}Ly6C^{hi} monocytes contribute to the enhanced immunity displayed by *Atg16L1*^{HM} mice, we generated *Atg16L1*^{HM}*Ccr2*$^{-/-}$ mice in which the chemokine receptor necessary for their recruitment during *C. rodentium* infection is absent[38]. WT, *Ccr2*$^{-/-}$, and *Atg16L1*^{HM}*Ccr2*$^{-/-}$ mice all displayed higher *C. rodentium* burden throughout the course of infection compared to *Atg16L1*^{HM} mice, with a 140 fold difference in bacterial burden between *Atg16L1*^{HM}*Ccr2*$^{-/-}$ and *Atg16L1*^{HM} mice at day 15 post infection (Figure 6c,d). The disease severity observed in these two groups was also markedly different (Figure 6e). WT, *Ccr2*$^{-/-}$, and *Atg16L1*^{HM}*Ccr2*$^{-/-}$ mice all show decreased colon length (Figure 6f) and increased dissemination to the liver (Figure 6g) compared to *Atg16L1*^{HM} mice at day 9 post infection. The intestinal inflammation at day 15 post infection in *Ccr2*$^{-/-}$ and *Atg16L1*^{HM}*Ccr2*$^{-/-}$ mice was comparable to WT mice, with *Atg16L1*^{HM} mice showing both reduced levels of crypt hyperplasia and intestinal pathology score (Figure 6h–j). These results support a model in which monocyte recruitment contributes to an antimicrobial and tissue regenerative response downstream of *Atg16L1* mutation in the colon.

DISCUSSION

Aberrant reactions to the microbiota is implicated in a range of disorders including IBD, yet a certain degree of responsiveness is necessary for host defense towards bona fide pathogens that access the gastrointestinal tract. We found that autophagy proteins in the colon suppress spontaneous activation of IFN-I signaling by the microbiota. Although our studies reveal a beneficial consequence of this enhanced activity, an IFN-I signature is a hallmark of several autoimmune diseases. Our findings indicate that mechanisms are in place to avoid spontaneous harmful IFN-I responses to the microbiota, which comes at the cost of antimicrobial immunity and tissue repair. Indeed, autophagy-deficiency has been shown to cause inappropriate IFN-I signaling in the absence of *DNaseII*, a gene mutated in systemic lupus erythematosus[42]. Given this relationship between IFN-I and autoimmune antibody responses, it will be interesting to examine how autophagy-deficiency impacts the generation of antibacterial IgG, previously shown to promote killing by phagocytes[43].

We cannot rule out non-autophagy functions of ATG16L1, ATG4B, and LC3B. However, our findings are consistent with the role of autophagy in mediating the degradation of MAVS[6–8]. Prior studies examining autophagy-deficient cells showed accumulation of MAVS and downstream signaling molecules shared with STING. The observation that

deletion of either MAVS or STING compromises the benefit of *Atg16L1* mutation suggests that both DNA and RNA moieties from the microbiota function as triggers. Our observations are further supported by the finding that RNA derived from the microbiota is recognized by RIG-I[44]. Recent studies indicate that metabolites from the microbiota potentiate IFN-I responses[45], and that autophagy inhibits TLR3 and TLR4 by degrading the adaptor TRIF, which can converge on a similar signaling pathway as cytosolic sensors[46–48]. A future direction would be to examine how specific ligands gain access to the epithelium to trigger immune responses and identify the relevant members of the microbiota. Our conventional mice are free of known viruses including MNV, but it will be important to determine whether viral members of the microbiota (including phages and endogenous retroviruses) contribute to the spontaneous IFN-I signaling we observe in autophagy-deficient mice.

The enhanced antimicrobial activity displayed by $Atg16L1^{HM}$ mice is dependent on infiltrating monocytes, yet we show that ATG16L1 in the intestinal epithelium mediates this increased resistance. Our results are most consistent with a model in which a heightened state of immunity is established by microbiota-triggered IFN-I signaling due to the absence of autophagy in the intestinal epithelium, and then autophagy-sufficient monocytes that are recruited to this microenvironment in response to *C. rodentium* acquire enhanced activity that accelerate the resolution of infection. This model highlights how autophagy proteins in the parenchyma can affect the local environment in a way that alters activation of infiltrating immune cells.

The mechanism revealed by this current study supports the emerging theme that autophagy proteins have a central role in balancing host defense and inflammation[2]. In the presence of a short-term threat to the gut, such as through *C. rodentium* infection or acute chemical injury, autophagy proteins have an adverse function. However, the benefit of autophagy inhibition is pathogen-specific, as demonstrated by the critical role of ATG5 and ATG16L1 in the epithelium during *Salmonella enterica* Typhimurium infection[49,50]. Also, our previous study showing that a persistent strain of MNV, but not a strain that causes an acute infection, triggers IBD pathologies in $Atg16L1^{HM}$ mice suggests that there is a long term cost to autophagy deficiency[10], and $Atg16L1^{HM}$ mice are not universally protected from acute bacterial infection as evidenced by their susceptibility to Staphylococcal infection[20]. In this context, it is notable that $Atg16L1^{T316A}$ mice become resistant to *C. rodentium* upon caspase-3 activation, because we showed that the same $Atg16L1^{T316A}$ mice are susceptible to MNV-induced pathology in the intestinal epithelium[26]. It is possible that this variant of *ATG16L1* was retained in the human population because of its immunomodulatory properties, which can be beneficial or detrimental depending on the circumstance. We suggest that understanding the cost-benefit of autophagy function in immunity will inform the therapeutic application of autophagy modulators and predict how autophagy gene variants affect the course of inflammatory and infectious diseases.

METHODS

Mice

Age and gender matched 8–12 week old mice on the C57BL/6J background were used as WT controls unless stated otherwise and bred onsite. $Atg16L1^{HM}$, $Atg16L1^{T316A}$,

Atg16L1$^{f/f}$ *Villin*^{cre}, *Atg16L1*$^{f/f}$ *Cdllc*^{cre}, and *LC3b*$^{-/-}$ mice were previously described[12,20,25,26]. *Atg4b*$^{-/-}$ mice were generously provided by Skip Virgin (Washington University School of Medicine)[51]. For single allele autophagy mutants, we used *Atg16L1*$^{HM/+}$, *Atg4b*$^{+/-}$, and LC3b$^{+/-}$ breeders to generate *Atg16L1*$^{HM/HM}$ and *Atg4b*$^{-/-}$ mice with their respective homozygous WT littermate controls (*Atg16L1*$^{+/+}$ and *Atg4b*$^{+/+}$). *Atg16L1*$^{f/f}$ *Villin*^{cre} and *Atg16L1*$^{f/f}$ *Cdllc*^{cre} mice were generated along with *Atg16L1*$^{f/f}$ littermates by breeding Cre-positive and negative *Atg16L1*$^{f/f}$ mice. *Ifnar*$^{-/-}$, *Ccr2*$^{-/-}$, *Mavs*$^{-/-}$, *Sting*$^{-/-}$, and *Caspase1.11*$^{-/-}$ mice were purchased from Jackson Laboratory and crossed to *Atg16L1*^{HM} mice to generate double mutants. For these compound mutants, we fixed the *Atg16L1*^{HM} allele first, then generated littermates that were homozygous knockout and wild-type for the other allele. Using the *Ifnar*-deficient mice as an example, *Atg16L1*$^{HM/HM}$*Ifnar*$^{+/-}$ mice were bred to each other through a trio mating scheme to generate *Atg16L1*$^{HM/HM}$*Ifnar*$^{+/+}$ and *Atg16L1*$^{HM/HM}$*Ifnar*$^{-/-}$ mice for experiments. To increase the number of mice analyzed, experiments were supplemented with progeny generated from *Atg16L1*$^{HM/HM}$*Ifnar*$^{-/-}$ breeder pairs. *Mavs*$^{-/-}$ mice are on a mixed C57BL/6 and 129/SvEv background and were bred to wild-type C57BL/6J mice to generate *Mavs*$^{+/-}$ mice, which were crossed to each other to generate controls for *Atg16L1* and *Mavs* double mutants that were generated by breeding *Atg16L1*^{HM}*Mavs*$^{+/-}$ mice, similar to other compound mutants. Experimental groups were established based off of genotype and infection status. All other aspects were randomized. Blinding was used during data collection by assigning numbers in place of genotype and infection status to mice in the studies. The number of animals used in the experiments in this study is estimated based on a power analysis with the following assumptions: standard deviation will be ~20% of the mean, p-value will be under 0.05 when the null hypothesis is false, the effect size (Cohen's d) is between 1.0–2.0. The minimal number of mice required under these conditions ranges between 5–38 for in vivo experiments depending on the assay. Additionally, we have carefully chosen the sample size based on empirical evidence of what is necessary for interpretation of the data and statistical significance. All animal studies were performed according to approved protocols by the NYU School of Medicine Institutional Animal Care and Use Committee (IACUC).

Bacterial infection

C. rodentium strain DBS100[12] was grown overnight in Luria-Bertani broth with shaking at 37°C and diluted 1:100 followed by an additional 3 hours of growth until bacteria were at an optical density of 2. Bacterial density was confirmed by dilution plating. Mice were inoculated by oral gavage with 2×10^9 cfu resuspended in 100 μl PBS. Severity of disease was quantified through a scoring system in which individual mice received a score of 1 for each of the following: hunched posture, inactivity, ruffled fur, and diarrhea. Mice received an additional score between 0 and 2 for weight loss calculated as percent of initial body weight, with a score of 0 = 0%–5%, 0.5 = 6%–10%, 1 = 11%–15%, 1.5 = 16%–20%, and 2 = greater than 20% loss. For quantification of bacterial shedding and dissemination, stool pellets or livers from individual mice were weighed, homogenized in PBS, and plated in serial dilutions on MacConkey agar. For caspase-3 activation, 50 mg kg^{-1} PAC-1 (APExBIO) was administered by oral gavage once a day for 3–5 days prior to C. *rodentium* infection.

Gnotobiotics

Previously described germ-free WT and *Atg16L1*^{HM} mice[12] were maintained in flexible film isolators and absence of fecal bacteria and fungi was confirmed by aerobic culture in brain heart infusion, sabaraud, and nutrient broth (Sigma), and qPCR for bacterial 16S and eukaryotic 18S ribosomal RNA genes through sampling of stool from individual cages in each isolator on a monthly basis. Mice were transferred into individually ventilated Tecniplast ISOcages for DSS treatment to maintain sterility under positive air pressure. For microbiota reconstitution experiments, stool slurries were prepared by resuspending 2–3 fecal pellets into 2mL of PBS and passing through a 40uM filter. Germ-free mice were gavaged with 200uL of stool slurries prior to transfer into ISOcages. Intestinal flora was allowed to stabilize for 3 weeks before mice were infected with C. *rodentium*.

Tissue collection and microscopy

Hematoxylin and eosin (H&E)-stained colonic sections were prepared as previously described from mice that were euthanized by cervical dislocation to preserve the integrity of intestinal tissue[12]. Severity of tissue pathology was blindly quantified by a pathologist (R.X.). Mice received a pathology score between 0 and 3 for crypt abscess, hyperplasia, mucin depletion, and for crypt loss and damage. A score of 0= negative pathology, 1= mild, 2= moderate, and 3 =severe pathology for the indicated fields. The length of at least 30 crypts per mouse was measured for crypt hyperplasia. Mean values were calculate for each mouse and used as individual data points. For immunohistochemistry (IHC), formalin fixed paraffin-embedded sections were deparaffinized online and antigen retrieved in Ventana Cell Conditioner 2 (Citrate). Endogenous peroxidase activity was blocked with hydrogen peroxide. Unconjugated polyclonal rabbit anti-mouse phospho-STAT1 (Cell Signaling Technology) and unconjugated rabbit anti-mouse Ki67 (M3062) (Spring Biosciences) were used and detected with anti-rabbit, horseradish peroxidase conjugated multimer and visualized with 3,3 diaminobenzidene and enhanced with copper sulfate. For Ki67 quantification, 10 images were collected per mouse, and from each image 3 crypts were quantified. Mean values were calculate from 30 images for each mouse and used as individual data points. For p-STAT1 quantification, the number of positive cells was quantified throughout the whole colon section. Two sections were quantified per mouse with mean values calculated for each mouse and used as individual data points. Imaging was performed on the Evos FL Color imaging microscope. All analyses of slides were performed blind and quantified using ImageJ software.

RNA isolation and qPCR

2mm colonic tissue, and 25mg heart, liver, lung, and MLN were washed and cut open (when appropriate), then suspended in 700uL of RLT buffer (Mini RNeasy Kit) and homogenized using TissueRuptor (Qiagen). RNA was then isolated using the RNeasy Mini Kit (Qiagen). As per manufacturer's instructions, DNase treatment was performed using RNeasy DNase kit (Qiagen) and protocol. cDNA synthesis was performed using ProtoScript M-MuLV First Strand cDNA synthesis kit (New England Biolabs) and Random Primers. qPCR was performed on a Roche480II Lightcycler using the following primers: *Gapdh* forward 5′tggccttccgtgttcctac 3′, *Gapdh* reverse 5′ gagttgctgttgaagtcgca3′, *Mx2* forward

5′ccagttcctctcagtcccaagatt 3′, and *Mx2* reverse 5′tactggatgatcaagggaacgtgg 3′, *OasL2* forward 5′ggatgcctgggagagaatcg 3′, and *OasL2* reverse 5′tcgcctgctcttcgaaactg 3′. Relative expression of the respective genes to *Gapdh* expression was calculated using the $\Delta\Delta C_T$ method and values were expressed as fold change normalized to uninfected WT mice.

Flow cytometry and RNA purification

To isolate immune cells from the lamina propria of the large intestine, small pieces of colon were washed with Hank's balanced salt solution (HBSS) and incubated at 37°C with shaking in HBSS containing 1 mM dithiothreitol (DTT) and 5 mM EDTA for 15 min, 1 mM EDTA HBSS for 10 min, washed with HBSS, and then incubated in HBSS containing 0.1 u/ml dispase (Worthington Biochemical), 0.1 mg/ml DNase (Sigma-Aldrich), and 1 mg/ml collagenase (Roche) for 25 min. Digested tissues were filtered and washed twice with RPMI containing 10% fetal calf serum (FCS). Isolated cells were resuspended in 40% Percoll (Pharmacia Biotech), layered onto 80% Percoll, and centrifuged at room temperature at 2,200 rpm for 20 min. Cells were recovered from the interphase and washed with RPMI containing 10% FCS. For T cell and innate lymphoid cell (ILC) subset profiling, cells were stimulated for 4 hours with a cell stimulation cocktail of PMA, ionomycin, brefeldin A, and monensin from eBioscience. Stimulated cells were stained for surface markers CD4 (RM4-5), CD8α (53-6.7), CD19 (6D5), CD11b (M1/70), TCRβ (H57-597), and CD90.2 (53-2.1), and intracellular markers IFNγ (XMG1.2) and IL-17a (TC11-18H10.1) from Biolegend, and IL-13 (ebio13A) and IL-22(1H8PWSR) from ebiosciences. A fixable live/dead stain from Biolegend was used to exclude dead cells. For profiling infiltrating monocytes, macrophages, and dendritic cells, isolated cells were stained with antibodies against surface markers CD103(2E.7), CD11b (M1/70), CD11c(N418), CD115(9-4D2-1E4), Ly6C(HK1.4), Ly6G(1A8) F4/80(BM8), MHC-II(M5/114.15.2), Galectin 9(108A2), Xcr1(zet) and live/dead viability stain. All antibodies were from Biolegend. To sort inflammatory monocytes from the isolated lamina propria, cells were stained for 1 hour at 4C for surface markers TCRβ (H57-597), CD19(6D5), CD103 (2E5), Ly6G(IA8), Cd11b (M1/70), Ly6C (HK1.4), FC block, and Dapi for viability stain (all antibodies were from Biolegend). Infiltrating monocytes were defined as $Dapi^-$, $TCR\beta^-$, $CD19^-$, $CD103^-$, $Ly6G^-$, $Cd11b^+$, $Ly6C^+$. Isolated lamina propria cells were resuspended in FCS then sorted directly into Trizol LS reagent (Life technologies) using a Coulter MoFlo XDP flow cytometry as well as the expertise and services of the NYU Langone Cytometry and Cell Sorting Laboratory. An initial RNA purification process was performed by first adding 200uL of chloroform to cells sorted into trizol LS. The aqueous phase was collected and 7.5ug of linear acrylamide (Ambion) was added and gently mixed. RNA was precipitated with one volume of 100% isopropanol at −20C for 1 hour then pelleted at full speed for 30 min, 4C. Pellet was washed with 75% ethanol, then re-pelleted at full speed, 5 min, 4C. Pellet was dried for 15 min at room temp and resuspended in 87.5uL of H2O. RNA was then isolated using RNeasy Mini kit (Qiagen).

16S library preparation and sequencing analysis

DNA isolation from stool samples was done using the NucleospinSoil Kit (Macherey-Nagel). Bacterial 16S rRNA gene was amplified at the V4 region using primer pairs[52] and paired-end amplicon sequencing was performed on the Illumina MiSeq system. Sequencing

reads were processed using the DADA2 pipeline in the QIIME2 software package[53]. Taxonomic assignment was performed against the Silva v132 database. Beta diversity was calculated using Bray Curtis distance. Principle Coordinate Analysis (PCoA) was performed on the Bray Curtis distance matrix and visualized with EMPeror[54].

RNA deep sequencing

cDNA libraries were prepared with the Ovation Ultralow RNA-seq System V2 (NuGEN) and sequenced on Illumina's HIseq platform using a paired end protocol at the NYU Genomics Core. On average, each sample yielded 32 million paired reads, which passed FASTQC quality control. Sequencing data was processed using Tuxedo suite; reads were aligned with TopHat v2.1.1 against UCSC mm10 genome assembly resulting in an average of 20 million aligned pairs per sample, and normalized read counts were calculated using Cufflinks v2.2.1 against the same reference genome. Differential gene expression was determined with Cuffdiff and gene ontology analysis performed using QIAGEN's Ingenuity Pathway Analysis (IPA, QIAGEN, Red Wood city, CA).

Western blot

2mm of proximal colonic tissue was cut open and washed with PBS, then suspended in T-PER Tissue Protein Extraction Reagent (Thermo-Scientific) containing 10X protease inhibitor (Santa Cruz Biotechnologies) and homogenized using TissueRuptor. Tissue homogenate was then pelleted twice at 10,000g x 10 min, 4C. Protein concentration in the supernatant was measured by Bradford assay and reduced using 4X Laemmli buffer containing b-mercapotethanol at 95C for 5 min. Due to similar molecular weights between MAVS, STING, ATG16L1, and β-actin, parallel gels were equally loaded, and equivalently processed. For gel electrophoresis, 20 to 30ug of protein were run at 120V for 1 hour using a 4–12% gradient protein gel (BioRad), electrophoresis chamber, and running buffer. Protein was then transferred to an Immun-Blot PVDF membrane through Bio-Rad semi-dry transfer apparatus for 1 hour, 12V constant. Membrane was incubated for 30 minutes with 5% Non-fat dairy milk, and mouse anti-β-actin (Abcam) at 1:1000, polyclonal rabbit anti- MAVS (Cell signaling) at 1:1000, mouse anti-ATG16L1 (MBL) at 1:1000 and polyclonal rabbit anti-STING (Cell signaling) at 1:1000 were probed overnight at 4C. Specificity of MAVS and STING antibodies were confirmed using lysates from *Mavs*$^{-/-}$ and *Sting*$^{-/-}$ mice, respectively. Membranes were washed 3 times for 5 minutes and probed with secondary antibody rabbit-anti mouse HRP and goat anti-rabbit HRP antibodies for 1 hour at RT. After additional washing, protein was then detected using Thermo Super Signal West Pico Chemiluminescent Substrate and imaged using Bio-Rad ChemiDoc XRS imaging system. β-actin, ATG16L1, and STING band intensity were quantified using single band analysis while MAVS protein intensity was quantified using complete lane analysis.

Dextran sodium sulfate treatment

Conventional mice were given 5% DSS (TdB consultancy) for 7 days and both survival and weight loss was measured over time. Germ-free mice were given 3% or 5% DSS and delivered in filter-sterilized water containing ampicillin (1 g l^{-1}; American bioanalytical), vancomycin (0.5 g l^{-1}; MP biomedicals), neomycin (1 g l^{-1}; Sigma), metronidazole (1 g l^{-1}; Sigma) and 1% sucrose (Fisher). Antibiotic-containing water was replaced at least once a

week. After DSS treatment, mice received regular or antibiotic-containing drinking water for the remainder of the experiment.

Statistical analysis

All analyses except for RNA-seq data used Graphpad Prism v.7. An unpaired two-tailed *t*-test was used to evaluate differences between two groups where data was distributed normally with equal variance between conditions. An analysis of variance (ANOVA) with Holm–Sidak multiple comparisons test was used to evaluate experiments involving multiple groups. The log-rank Mantel–Cox test was used for comparison of mortality curves.

Data Sharing and Availability

The data that support the findings of this study are available from the corresponding author upon request. FASTQ files corresponding to the RNA-seq data have been deposited in a public database (RNA-seq GEO accession # GSE115025, 16S GEO accession # GSE116491).

Supplementary Material

Refer to Web version on PubMed Central for supplementary material.

Acknowledgments

We wish to thank the following NYU facilities for use of their instruments and technical assistance: Microcopy Core (RR023704), Histopathology and Immunohistochemistry Core (P30CA016087, NIH S10 OD010584-01A1, and S10 OD018338-01), the Cytometry and Cell Sorting Laboratory (P30CA016087), the Genome Technology Center (P30CA016087), and the Gnotobitoic Facility (Colton Center for Autoimmunity). This work was supported by US National Institute of Health (NIH) grants R01 HL123340 (K.C.), R01 DK093668 (K.C.), R01 DK103788 (K.C.), R01 AI121244 (K.C.), F31 DK111139 (P.K.M.), and T32 AI100853 (E.R.); Faculty Scholar grant from the Howard Hughes Medical Institute (K.C.), Advanced Research Grant from the Merieux Institute (K.C.), Rainin Foundation Innovator Award (K.C.), Stony Wold-Herbert Fund (K.C.), and philanthropy from Bernard Levine (K.C.); and Crohn's & Colitis Foundation Research Fellowship Award (A.M.). K.C. is a Burroughs Wellcome Fund Investigator in the Pathogenesis of Infectious Diseases.

References

1. Ramanan D, Cadwell K. Intrinsic Defense Mechanisms of the Intestinal Epithelium. Cell Host Microbe. 2016; 19:434–441. [PubMed: 27049583]
2. Cadwell K. Crosstalk between autophagy and inflammatory signalling pathways: balancing defence and homeostasis. Nat Rev Immunol. 2016
3. Tal MC, et al. Absence of autophagy results in reactive oxygen species-dependent amplification of RLR signaling. Proc Natl Acad Sci U S A. 2009; 106:2770–2775. [PubMed: 19196953]
4. Jounai N, et al. The Atg5 Atg12 conjugate associates with innate antiviral immune responses. Proc Natl Acad Sci U S A. 2007; 104:14050–14055. [PubMed: 17709747]
5. Liang Q, et al. Crosstalk between the cGAS DNA sensor and Beclin-1 autophagy protein shapes innate antimicrobial immune responses. Cell Host Microbe. 2014; 15:228–238. [PubMed: 24528868]
6. Lei Y, et al. The mitochondrial proteins NLRX1 and TUFM form a complex that regulates type I interferon and autophagy. Immunity. 2012; 36:933–946. [PubMed: 22749352]
7. Zhao Y, et al. COX5B regulates MAVS-mediated antiviral signaling through interaction with ATG5 and repressing ROS production. PLoS Pathog. 2012; 8:e1003086. [PubMed: 23308066]
8. Mathew R, et al. Functional role of autophagy-mediated proteome remodeling in cell survival signaling and innate immunity. Molecular cell. 2014; 55:916–930. [PubMed: 25175026]

9. Cadwell K, et al. A key role for autophagy and the autophagy gene Atg16l1 in mouse and human intestinal Paneth cells. Nature. 2008; 456:259–263. [PubMed: 18849966]
10. Cadwell K, et al. Virus-plus-susceptibility gene interaction determines Crohn's disease gene Atg16L1 phenotypes in intestine. Cell. 2010; 141:1135–1145. [PubMed: 20602997]
11. Kernbauer E, Ding Y, Cadwell K. An enteric virus can replace the beneficial function of commensal bacteria. Nature. 2014; 516:94–98. [PubMed: 25409145]
12. Marchiando AM, et al. A deficiency in the autophagy gene Atg16L1 enhances resistance to enteric bacterial infection. Cell Host Microbe. 2013; 14:216–224. [PubMed: 23954160]
13. Grimm WA, et al. The Thr300Ala variant in ATG16L1 is associated with improved survival in human colorectal cancer and enhanced production of type I interferon. Gut. 2015
14. Lopez CA, et al. Virulence factors enhance Citrobacter rodentium expansion through aerobic respiration. Science. 2016; 353:1249–1253. [PubMed: 27634526]
15. Lupp C, et al. Host-mediated inflammation disrupts the intestinal microbiota and promotes the overgrowth of Enterobacteriaceae. Cell Host Microbe. 2007; 2:119–129. [PubMed: 18005726]
16. Hoffmann C, et al. Community-wide response of the gut microbiota to enteropathogenic Citrobacter rodentium infection revealed by deep sequencing. Infect Immun. 2009; 77:4668–4678. [PubMed: 19635824]
17. Hwang S, et al. Nondegradative role of Atg5-Atg12/ Atg16L1 autophagy protein complex in antiviral activity of interferon gamma. Cell host & microbe. 2012; 11:397–409. [PubMed: 22520467]
18. Choi J, et al. The parasitophorous vacuole membrane of Toxoplasma gondii is targeted for disruption by ubiquitin-like conjugation systems of autophagy. Immunity. 2014; 40:924–935. [PubMed: 24931121]
19. Marino G, et al. Autophagy is essential for mouse sense of balance. The Journal of clinical investigation. 2010; 120:2331–2344. [PubMed: 20577052]
20. Maurer K, et al. Autophagy Mediates Tolerance to Staphylococcus aureus Alpha-Toxin. Cell Host Microbe. 2015; 17:429–440. [PubMed: 25816775]
21. Cann GM, et al. Developmental expression of LC3alpha and beta: absence of fibronectin or autophagy phenotype in LC3beta knockout mice. Dev Dyn. 2008; 237:187–195. [PubMed: 18069693]
22. Chen ZH, et al. Autophagy protein microtubule-associated protein 1 light chain-3B (LC3B) activates extrinsic apoptosis during cigarette smoke-induced emphysema. Proceedings of the National Academy of Sciences of the United States of America. 2010; 107:18880–18885. [PubMed: 20956295]
23. Inoue J, et al. Autophagy in the intestinal epithelium regulates Citrobacter rodentium infection. Arch Biochem Biophys. 2012; 521:95–101. [PubMed: 22475450]
24. Pott J, Kabat AM, Maloy KJ. Intestinal Epithelial Cell Autophagy Is Required to Protect against TNF-Induced Apoptosis during Chronic Colitis in Mice. Cell Host Microbe. 2018; 23:191–202e194. [PubMed: 29358084]
25. Hubbard-Lucey VM, et al. Autophagy gene atg16l1 prevents lethal T cell alloreactivity mediated by dendritic cells. Immunity. 2014; 41:579–591. [PubMed: 25308334]
26. Matsuzawa-Ishimoto Y, et al. Autophagy protein ATG16L1 prevents necroptosis in the intestinal epithelium. J Exp Med. 2017
27. Murthy A, et al. A Crohn's disease variant in Atg16l1 enhances its degradation by caspase 3. Nature. 2014; 506:456–462. [PubMed: 24553140]
28. Lassen KG, et al. Atg16L1 T300A variant decreases selective autophagy resulting in altered cytokine signaling and decreased antibacterial defense. Proc Natl Acad Sci U S A. 2014; 111:7741–7746. [PubMed: 24821797]
29. Zhang H, et al. Myeloid ATG16L1 Facilitates Host-Bacteria Interactions in Maintaining Intestinal Homeostasis. J Immunol. 2017; 198:2133–2146. [PubMed: 28130498]
30. Gao P, et al. The Inflammatory Bowel Disease-Associated Autophagy Gene Atg16L1T300A Acts as a Dominant Negative Variant in Mice. J Immunol. 2017; 198:2457–2467. [PubMed: 28202618]

31. Putt KS, et al. Small-molecule activation of procaspase-3 to caspase-3 as a personalized anticancer strategy. Nature chemical biology. 2006; 2:543–550. [PubMed: 16936720]
32. Konno H, Konno K, Barber GN. Cyclic dinucleotides trigger ULK1 (ATG1) phosphorylation of STING to prevent sustained innate immune signaling. Cell. 2013; 155:688–698. [PubMed: 24119841]
33. Saitoh T, et al. Atg9a controls dsDNA-driven dynamic translocation of STING and the innate immune response. Proc Natl Acad Sci U S A. 2009; 106:20842–20846. [PubMed: 19926846]
34. Moretti J, et al. STING Senses Microbial Viability to Orchestrate Stress-Mediated Autophagy of the Endoplasmic Reticulum. Cell. 2017; 171:809–823e813. [PubMed: 29056340]
35. Prabakaran T, et al. Attenuation of cGAS-STING signaling is mediated by a p62/SQSTM1-dependent autophagy pathway activated by TBK1. Embo J. 2018; 37
36. Sun L, et al. Type I Interferons Link Viral Infection to Enhanced Epithelial Turnover and Repair. Cell Host Microbe. 2014
37. Kamada N, et al. Regulated virulence controls the ability of a pathogen to compete with the gut microbiota. Science. 2012; 336:1325–1329. [PubMed: 22582016]
38. Kim YG, et al. The Nod2 Sensor Promotes Intestinal Pathogen Eradication via the Chemokine CCL2-Dependent Recruitment of Inflammatory Monocytes. Immunity. 2011
39. Van den Bossche J, O'Neill LA, Menon D. Macrophage Immunometabolism: Where Are We (Going)? Trends in immunology. 2017; 38:395–406. [PubMed: 28396078]
40. Saitoh T, et al. Loss of the autophagy protein Atg16L1 enhances endotoxin-induced IL-1beta production. Nature. 2008; 456:264–268. [PubMed: 18849965]
41. Liu Z, et al. Role of inflammasomes in host defense against Citrobacter rodentium infection. J Biol Chem. 2012; 287:16955–16964. [PubMed: 22461621]
42. Lan YY, Londono D, Bouley R, Rooney MS, Hacohen N. Dnase2a deficiency uncovers lysosomal clearance of damaged nuclear DNA via autophagy. Cell reports. 2014; 9:180–192. [PubMed: 25284779]
43. Zeng MY, et al. Gut Microbiota-Induced Immunoglobulin G Controls Systemic Infection by Symbiotic Bacteria and Pathogens. Immunity. 2016; 44:647–658. [PubMed: 26944199]
44. Li XD, et al. Mitochondrial antiviral signaling protein (MAVS) monitors commensal bacteria and induces an immune response that prevents experimental colitis. Proceedings of the National Academy of Sciences of the United States of America. 2011; 108:17390–17395. [PubMed: 21960441]
45. Steed AL, et al. The microbial metabolite desaminotyrosine protects from influenza through type I interferon. Science. 2017; 357:498–502. [PubMed: 28774928]
46. Samie M, et al. Selective autophagy of the adaptor TRIF regulates innate inflammatory signaling. Nat Immunol. 2018; 19:246–254. [PubMed: 29358708]
47. Gentle IE, et al. TIR-domain-containing adapter-inducing interferon-beta (TRIF) forms filamentous structures, whose pro-apoptotic signalling is terminated by autophagy. FEBS J. 2017; 284:1987–2003. [PubMed: 28453927]
48. Yang Q, et al. TRIM32-TAX1BP1-dependent selective autophagic degradation of TRIF negatively regulates TLR3/4-mediated innate immune responses. PLoS Pathog. 2017; 13:e1006600. [PubMed: 28898289]
49. Benjamin JL, Sumpter R Jr, Levine B, Hooper LV. Intestinal Epithelial Autophagy Is Essential for Host Defense against Invasive Bacteria. Cell Host Microbe. 2013; 13:723–734. [PubMed: 23768496]
50. Conway KL, et al. Atg16l1 is required for autophagy in intestinal epithelial cells and protection of mice from Salmonella infection. Gastroenterology. 2013; 145:1347–1357. [PubMed: 23973919]

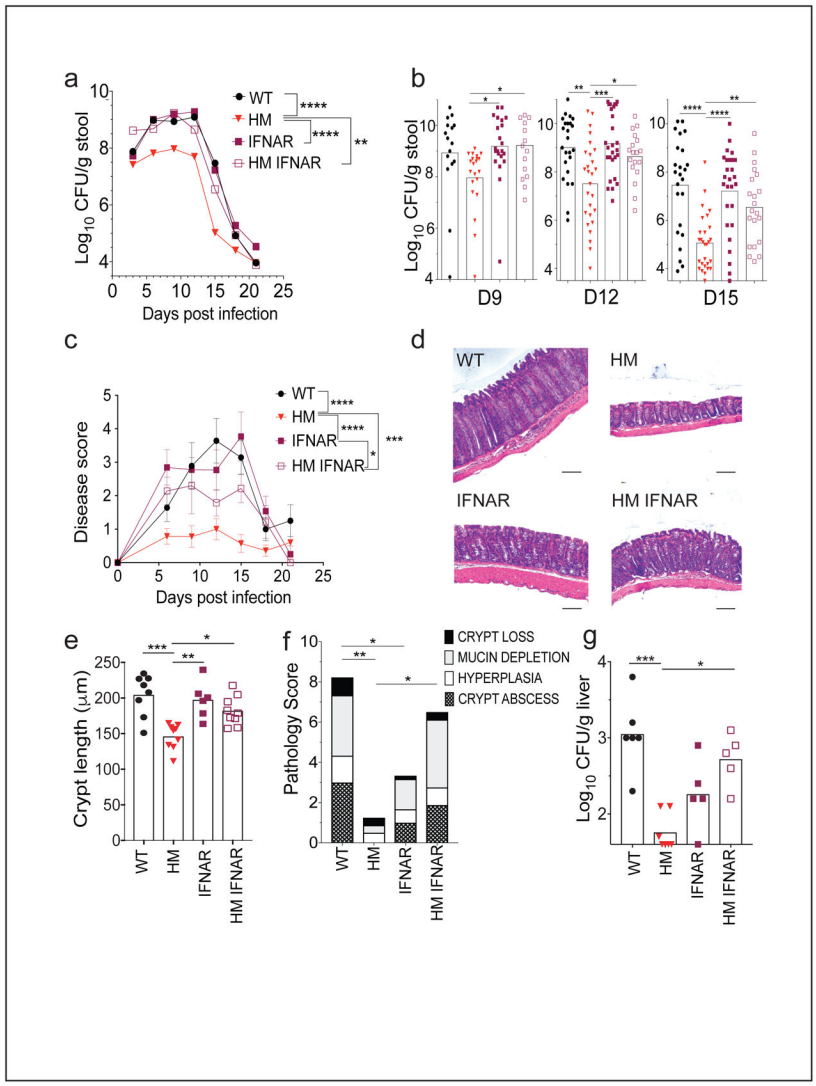

Figure 1. Protection conferred by ATG16L1 inhibition is dependent on the IFN-I pathway

(a) Mean colony forming units (CFUs) recovered from stool over time from WT (n=22), *Atg16L1*^{HM} (n=25), *Ifnar*$^{-/-}$(n=27), and *Atg16L1*^{HM}*Ifnar*$^{-/-}$ (n=21) mice inoculated with *C. rodentium*. 6 independent experiments were performed. **(b)** Quantification of bacterial burden in stool on indicated days from (a). **(c)** Quantification of disease over time for mice in (a). Disease score is a measurement of hunched posture, ruffled fur, immobility, and weight loss (See Methods). **(d–f)** Representative H&E-stained colonic sections from WT (n=8), *Atg16L1*^{HM}(n=9), *Ifnar*$^{-/-}$(n=6), and *Atg16L1*^{HM}*Ifnar*$^{-/-}$ (n=9) mice (d). Quantification of crypt hyperplasia (e), and cumulative pathology score (f) on day 15 post infection from 2 independent experiments. Scale bar=100μm. **(g)** Bacterial burden in the liver measured by CFUs per gram tissue. Data points in (a) and (c) and bars in (b), (e), (f), and (g) represent mean, and dots in (b) and (g) represent individual mice. Error bars in (c) and (e) represent SEM. ANOVA with Holm–Sidak multiple comparisons test was used to evaluate significance in all graphs for this figure. *p<0.05, **p<0.01, ***p<0.001, and ****p<0.0001 (Supplemental Table 2 lists exact p-values).

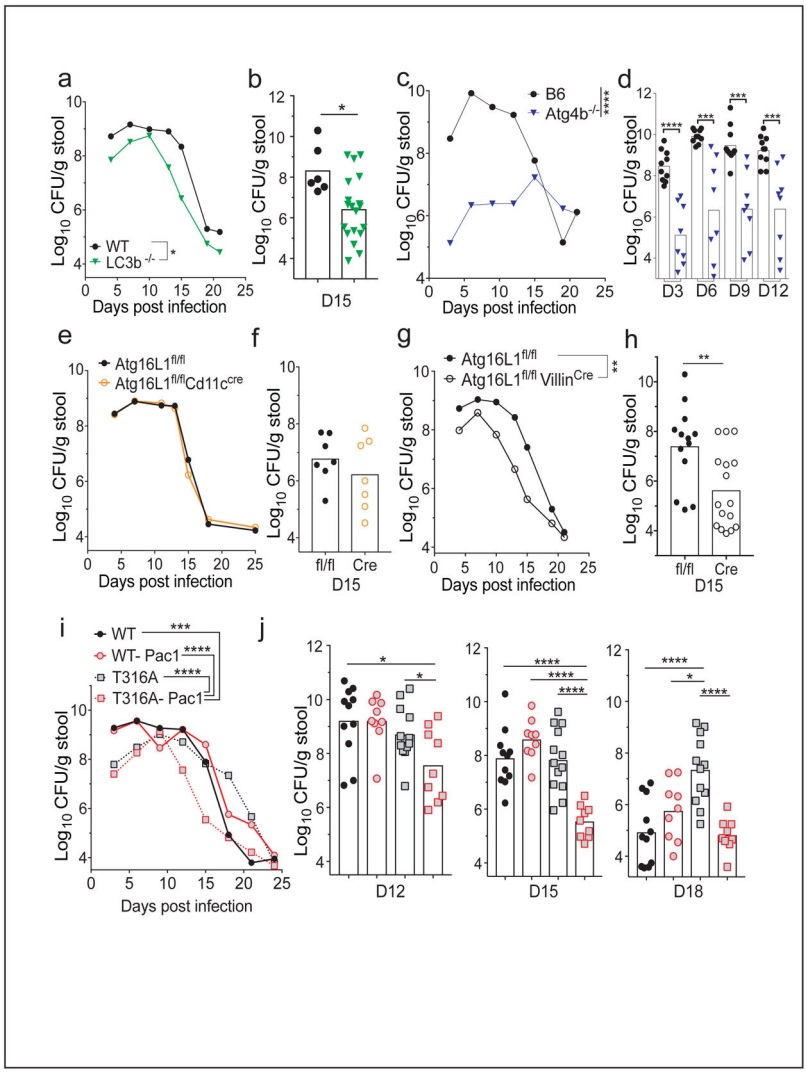

Figure 2. Different models of autophagy deficiency confer resistance to C. *rodentium* infection

(a) Mean colony forming units (CFUs) recovered from stool over time from WT (n=6) and LC3b$^{-/-}$ (n=19) mice inoculated with *C. rodentium*. 3 independent experiments were performed. **(b)** Quantification of bacterial burden in stool on day 15 post infection from (a). **(c)** Mean CFUs recovered from stool over time from WT (n=10) and Atg4b$^{-/-}$(n=8) mice inoculated with *C. rodentium*. 2 independent experiments were performed. **(d)** Quantification of bacterial burden in stool on indicated days from (c). **(e)** Mean CFUs recovered from stool over time from Atg16L1$^{fl/fl}$ (n=7) and Atg16L1$^{fl/fl}$Cdllc^{Cre} (n=8) mice inoculated with *C. rodentium*. 2 independent experiments were performed. **(f)** Quantification of bacterial burden in stool on day 15 post infection from (e). **(g)** Mean CFUs recovered from stool over time from Atg16L1$^{fl/fl}$ (n=13) and Atg16L1$^{fl/fl}$Villin^{Cre} (n=16) mice inoculated with *C. rodentium* from 4 independent experiments. **(h)** Quantification of bacterial burden in stool on day 15 post infection from (g). **(i)** Mean CFUs recovered from stool over time from WT (n=12), WT-Pac1 treated (n=10), Atg16L1^{T316A} (n=13), and Atg16L1^{T316A} Pac1 treated (n=9) mice inoculated with *C. rodentium*. 3 independent

experiments were performed. **(j)** Quantification of bacterial burden in stool on day 15 post infection from (i). Bars represent mean and dots represent individual mice. An unpaired two-tailed *t*-test was used to evaluate differences between two groups where data was distributed normally with equal variance between conditions (a–h). ANOVA with Holm–Sidak multiple comparisons test was used to evaluate significance for experiments involving multiple groups (i,j). *p<0.05, **p<0.01, ***p<0.001, and ****p<0.0001 (Supplemental Table 2 lists exact p-values).

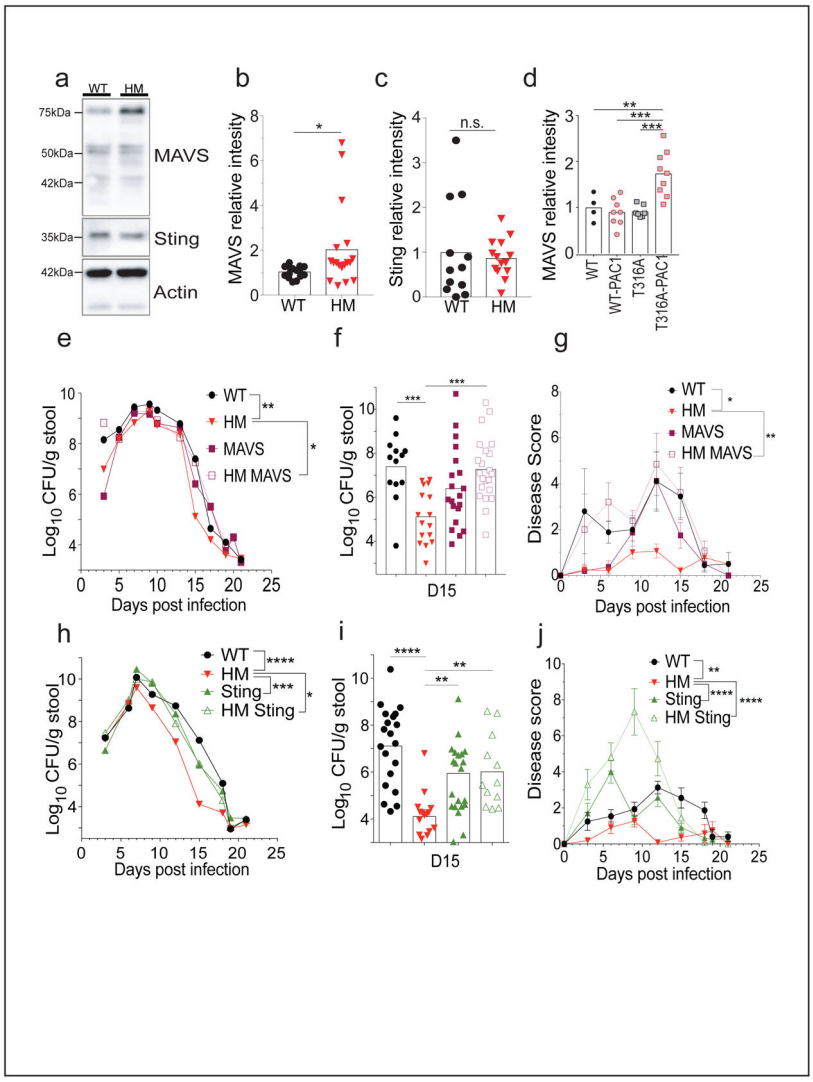

Figure 3. Protection conferred by ATG16L1 inhibition is dependent on MAVS and STING

(a–c) Representative Western blot (a) and quantification of MAVS (b) and STING (c) from colonic tissue of uninfected *Atg16L1*^{HM} (n=18) and WT (n=16) mice normalized to β-actin from 3 independent experiments. Relative intensity of MAVS protein was determined by complete lane analysis. Full-length original blots can be found in Supplemental Figure 4h. **(d)** Quantification of MAVS from colonic tissue of uninfected WT (n=5), *Atg16L1*^{T316A} (n=7), WT-Pac1 treated (n=8), and *Atg16L1*^{T316A}-Pac1 treated (n=9) mice. Protein is normalized to β-actin from 2 independent experiments. **(e–f)** Bacteria in stool over time (e) and on day 15 (f) from WT (n=13), *Atg16L1*^{HM} (n=19), *Mavs*$^{-/-}$ (n=20), and *Atg16L1*^{HM}*Mavs*$^{-/-}$ (n=26) mice inoculated with *C. rodentium*. 4 independent experiments were performed. **(g)** Quantification of disease over time for mice in (e). **(h–i)** Bacteria in stool over time (h) and on day 15 (i) from WT (n=20), *Atg16L1*^{HM} (n=16), *Sting*$^{-/-}$ (n=24), and *Atg16L1*^{HM}*Sting*$^{-/-}$ (n=24) mice inoculated with *C. rodentium*. **(j)** Quantification of disease over time for mice in (h). 3 independent experiments were performed. Data points in (e), (g), (h) and (j) and bars in (b), (c), (d), (f), and (i) represent mean. Error bars represent

SEM. Dots in (b), (c), (d), (f) and (i) represent individual mice. An unpaired two-tailed *t*-test was used to evaluate differences between two groups (b) and (c). ANOVA with Holm–Sidak multiple comparisons test was used to evaluate significance for experiments involving multiple groups (d–j). *p<0.05, **p<0.01, ***p<0.001, and ****p<0.0001 (Supplemental Table 2 lists exact p-values).

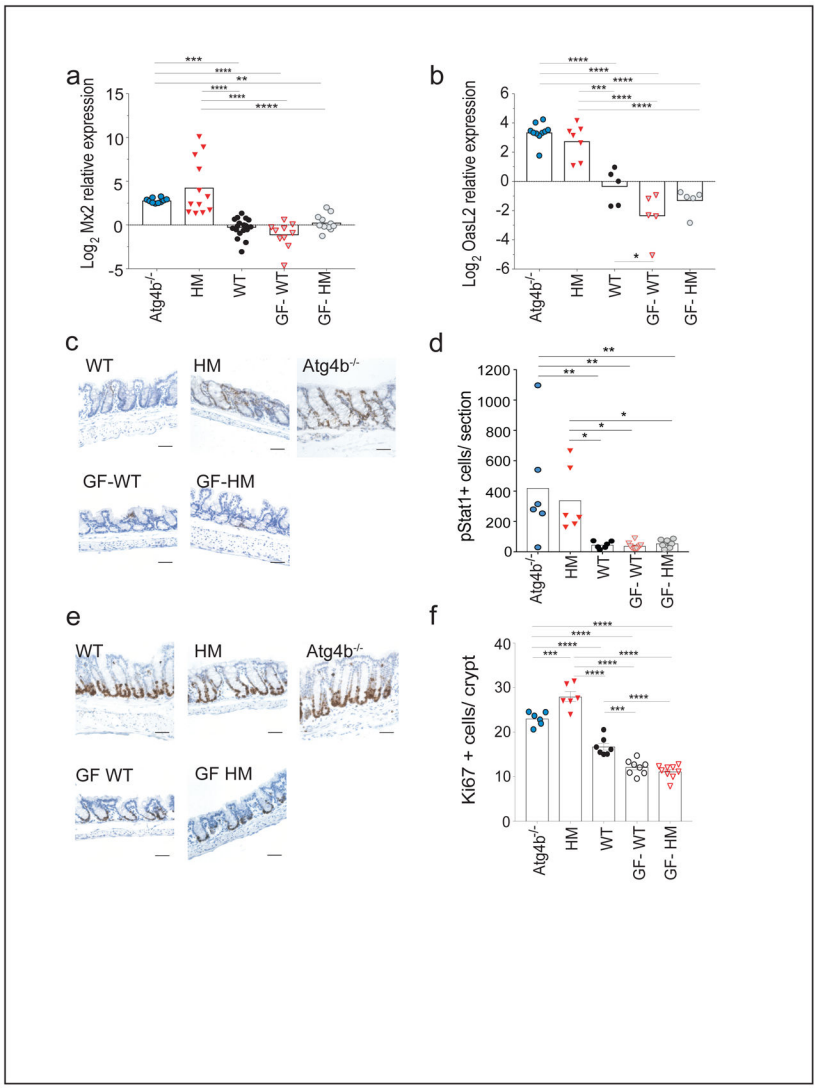

Figure 4. The type I IFN signature in colonic tissue of autophagy deficient mice is dependent on the microbiota

(a,b) qRT-PCR analyses of *Mx2* (a) and *OasL2* (b) expression relative to *Gapdh* in colonic tissue from uninfected *Atg4b*$^{-/-}$ (n=10), *Atg16L1*^{HM} (n=12), WT (n=15), germ-free (GF) WT (n=15), and GF *Atg16L1*^{HM} (n=15) mice from 4 independent experiments. **(c–f)** Representative immunohistochemistry (IHC) images and quantification of pStat1 (c,d) and Ki67 (e,f) staining in colonic tissue from *Atg4b*$^{-/-}$ (n=7), *Atg16L1*^{HM} (n=7), WT (n=6), germ-free (GF) WT (n=7), and GF *Atg16L1*^{HM} (n=10) mice. 2 independent experiments were performed. Bars in (a), (b), (d), and (f) represent mean. Error bars represent SEM. Scale bar=100μm. ANOVA with Holm–Sidak multiple comparisons test was used to evaluate significance in all graphs for this figure. *p<0.05, **p<0.01, ***p<0.001, and ****p<0.0001 (Supplemental Table 2 lists exact p-values).

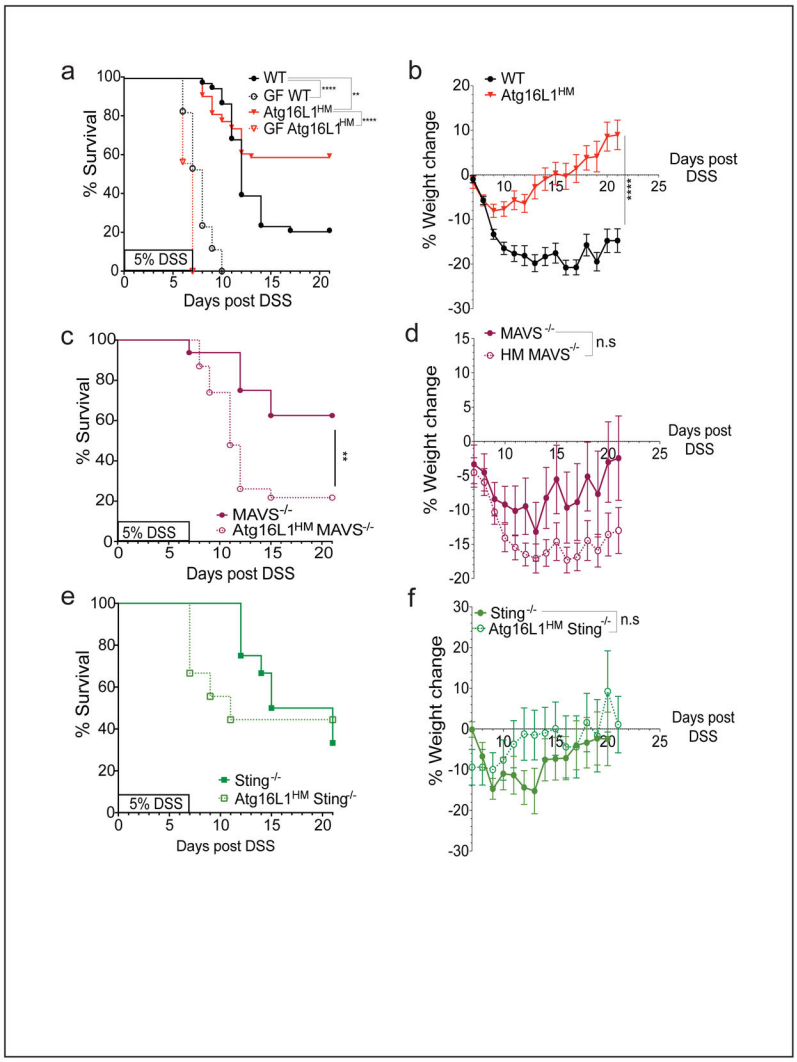

Figure 5. Autophagy deficiency protects against chemical injury of the intestine

(a,b) Survival (a) and change in body weight (b) of WT (n=38), *Atg16L1*^{HM} (n=35), germ-free WT (n=17), and germ-free *Atg16L1*^{HM} (n=16) mice receiving 5% dextran sodium sulfate (DSS) in drinking water for 7 days. **(c,d)** Survival (c) and change in body weight (d) of *Mavs*$^{-/-}$ (n=15) and *Atg16L1*^{HM}*Mavs*$^{-/-}$(n=25) mice receiving 5% DSS. **(e,f)** Survival (e) and change in body weight (f) of *Sting*$^{-/-}$(n=12) and *Atg16L1*^{HM}*Sting*$^{-/-}$ (n=10) mice receiving 5% DSS. At least 2 independent experiments were performed. Data points represent mean ± SEM in (b), (d), and (f). An unpaired two-tailed *t*-test was used to evaluate differences between two groups where data was distributed normally with equal variance between conditions (b), (d), and (f). The log-rank Mantel–Cox test was used for comparison of mortality curves (a), (c), and (e). **p<0.01, ***p<0.001, and ****p<0.0001 (Supplemental Table 2 lists exact p-values).

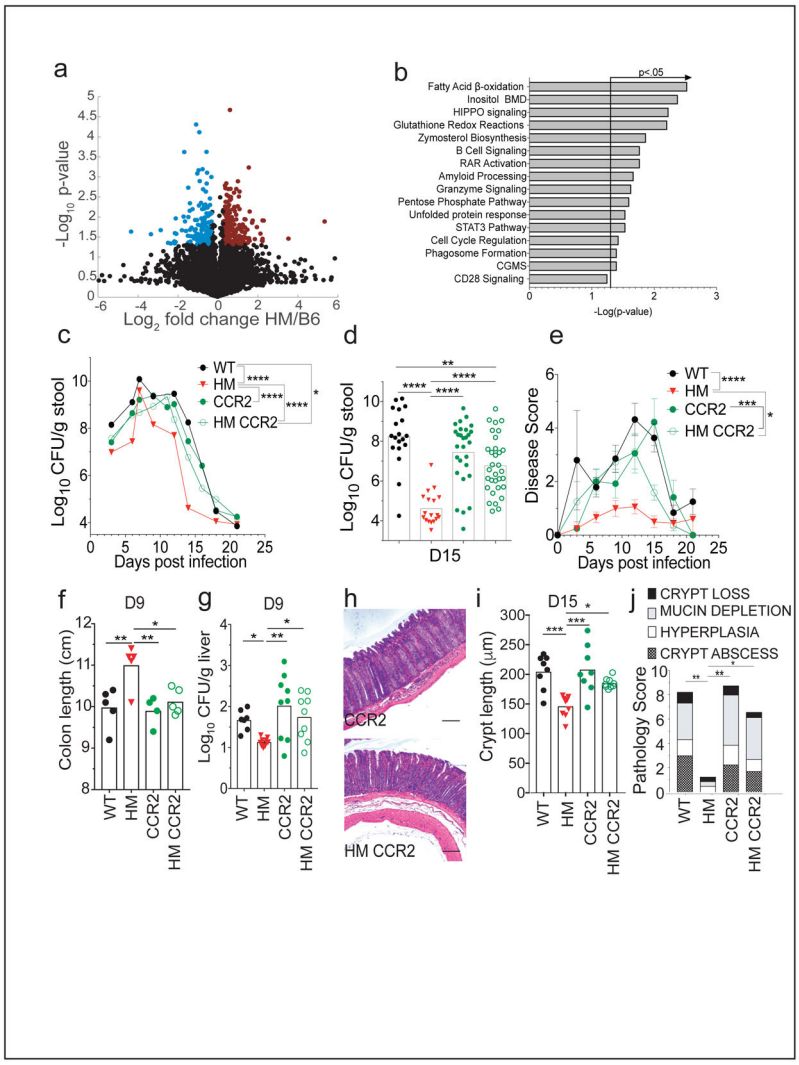

Figure 6. Protection conferred by *Atg16L1* mutation is associated with enhanced monocyte function

(a) RNAseq analysis was performed on monocytes harvested from WT and *Atg16L1*^{HM} mice on day 9 post *Citrobacter rodentium* infection. Volcano plot of all transcripts that mapped to the murine transcriptome show 404 differentially up-regulated genes in monocytes from *Atg16L1*^{HM} mice labeled in red and 402 downregulated genes labeled in blue. n= 4 mice/group. **(b)** Functional classification of differentially regulated genes from (a) by Ingenuity pathway analysis. The arrowed line marks where the p-value becomes less than 0.05 and highlights the pathways that are significantly different between WT and *Atg16L1*^{HM} transcriptional profiles. Inositol BMD= Inositol Biosynthesis, metabolism, and degradation, CGMS=cholecystokinin and gastrin-mediated signaling. **(c,d)** Bacteria recovered from stools over time (c) and on day 15 (d) from WT(n=19), *Atg16L1*^{HM}(n=18), *Ccr2*$^{-/-}$(n=29), and *Atg16L1*^{HM}*Ccr2*$^{-/-}$(n=22) mice inoculated with *C. rodentium*. 6 independent experiments were performed. **(e)** Quantification of disease over time for mice in (c). **(f)** Colon length of WT (n=5), *Atg16L1*^{HM} (n=4), *Ccr2*$^{-/-}$ (n=5), and *Atg16L1*^{HM}*Ccr2*$^{-/-}$ (n=5) mice infected at day 9 with C. rodentium infection from 1

experiment. **(g)** Bacterial burden in the liver measured by CFUs per gram tissue in WT (n=7), *Atg16L1*^{HM} (n=10), *Ccr2*$^{-/-}$ (n=9), and *Atg16L1*^{HM}*Ccr2*$^{-/-}$ (n=9) mice at day 9 post C. rodentium infection from 2 experiments. **(h–j)** Representative H&E-stained colonic sections (h), quantification of crypt length (i), and cumulative pathology sore (j) on day 15 post infection from WT (n=8), *Atg16L1*^{HM} (n=9), *Ccr2*$^{-/-}$ (n=8), and *Atg16L1*^{HM}*Ccr2*$^{-/-}$ (n=9) mice. 3 independent experiments were performed. Scale bar=100μm. Data points in (c), (e) and bars in (d), (f), (g), (i), and (j) represent mean. Error bars represent SEM. An unpaired two-tailed *t*-test was used to evaluate differences between two groups (b). ANOVA with Holm–Sidak multiple comparisons test was used to evaluate significance for experiments involving multiple groups (c–j). *p<0.05, **p<0.01, ***p<0.001, and ****p<0.0001 (Supplemental Table 2 lists exact p-values).